Small-x effects in heavy quark production

A. Dainese[a], K. J. Eskola[b], H. Jung[c], V. J. Kolhinen[b], K. Kutak[d,e], A. D. Martin[f], L. Motyka[c],
K. Peters[c,g], M. G. Ryskin[h], and R. Vogt[i,j]

[a] University of Padova and INFN, Padova, Italy

[b] Department of Physics, University of Jyväskylä, Jyväskylä, Finland

[c] Deutsches Elektronen-Synchroton DESY, Hamburg, FRG

[d] University of Hamburg, Hamburg, FRG

[e] Henryk Niewodnicznski Institute of Nuclear Physics, Polish Academy of Sciences, Poland

[f] Institute for Particle Physics Phenomenology, University of Durham, Durham, UK

[g] Department of Physics and Astronomy, University of Manchester, UK

[h] Petersburg Nuclear Physics Institute, Gatchina, St. Petersburg, Russia

[i] Lawrence Berkeley National Laboratory, Berkeley, CA, USA

[j] Physics Department, University of California, Davis, CA, USA

Abstract

We study small-x effects on heavy flavor production at the LHC in two approaches including nonlinear, saturation-motivated, terms in the parton evolution. One approach is based on collinear factorization, the other on k_T factorization. The prospects for direct experimental study of these effects in pp collisions at the LHC are discussed.

Coordinators: A. Dainese, H. Jung, and R. Vogt

1 Introduction

HERA data are used to constrain the small x, moderate Q^2 parton densities in two approaches. In the first, HERA F_2 data are refit using DGLAP evolution with the first nonlinear recombination terms. Recombination slows the evolution so that, after refitting the data, the gluon distribution is enhanced relative to that obtained by DGLAP alone. The resulting set of parton densities produces charm enhancement in pp collisions at the LHC. On the other hand, assuming k_T factorization, the unintegrated gluon distribution is determined from the HERA F_2^c data, the only inclusive HERA measurements which directly accesses the gluon density. Saturation effects are then included, reducing the small x gluon densities with little distinguishable effect on F_2. This approach leads instead to heavy flavor suppression at the LHC. After a short general introduction, both approaches and their predicted effects on heavy quark production are discussed in detail. Direct experimental study of these effects in pp collisions at the LHC may be able to differentiate between the two approaches.

2 Small-x partons, absorption and the LHC[1]

2.1 Partons densities at low x?

Almost nothing is known about the behaviour of partons at low x. There are essentially no data available for $x < 10^{-4}$ with Q^2 in the perturbative region and there is no reliable theory to extrapolate down in x.

In the Dokshitzer-Gribov-Lipatov-Altarelli-Parisi (DGLAP)-based [1–4] global analyses, small-x behaviour is driven by input distributions at a starting scale $Q = Q_0$. Usually these 'input' distributions are written in the form $x^{-\lambda}(1-x)^\eta$ where λ and η are free parameters fit to the data. So one can say nothing without data in the x region of interest. Moreover, there may be large low-x contributions to the gluon of the form $(\alpha_s \ln(1/x))^n$ – the so-called Balitsky-Fadin-Kuraev-Lipatov (BFKL) effects [5–8], beyond the DGLAP approximation.

---

[1] Authors: A.D. Martin and M.G. Ryskin

A. Dainese, K. J. Eskola, H. Jung, V. J. Kolhinen, K. Kutak, A. D. Martin, . . .
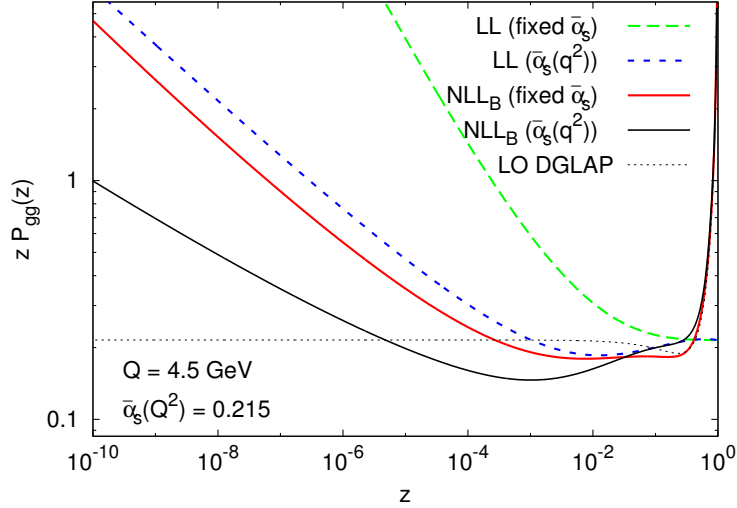
Fig. 1: The gluon-gluon splitting function, P_{gg}, with fixed and running coupling in the LL and resummed NLL BFKL approximations, compared with the LO DGLAP behaviour. The figure is taken from Ciafaloni et al. [9–14]. The subscript B refers to scheme B which ensures energy-momentum conservation in the splitting.

Thus it seems better to discuss low-x behaviour in terms of BFKL-evolution. However there are also problems here. The next-to-leading logarithm (NLL) corrections to the leading order (LO) BFKL (CCFM) amplitude are known to be very large and one needs to resum such corrections to obtain a relatively stable result. We cannot justify the perturbative QCD approach at low Q^2 so that the solution of the BFKL equation need to be matched to some non-perturbative amplitude at $Q = Q_0$. This non-perturbative distribution (analogous to the 'input' in the DGLAP case) is not known theoretically. Either it has to be fit to low x data or some phenomenological model such as a Regge-based parametrization has to be used.

After a reasonable resummation of the NLL corrections in the region where the starting virtuality Q_0 is not close to the final value of Q, $Q > Q_0$, the resummed BFKL amplitude turns out to be similar to that resulting from DGLAP evolution [9–14]. For example, the preasymptotic effects on the resummation of the gluon-gluon splitting function are so large that the NLL BFKL power growth only sets in for $z < 10^{-5}$, as can be seen from Fig. 1. Moreover, the behaviour of the convolution $P_{gg} \otimes g/g$, normalized to g, in the NNLO DGLAP and NLL approximations is exactly the same down to $z \sim 10^{-4}$ [15].

Thus, in practice, the DGLAP and BFKL based approaches are rather close to each other in the HERA kinematic regime. In both cases, the main problem is the low-x behaviour of the amplitude at $Q = Q_0$ where we need to phenomenologically determine possible non-perturbative contributions, power corrections and so on.

2.2 The puzzle of the $x^{-\lambda}$ behaviour

Since the BFKL amplitude grows as a power of x, $A \propto x^{-\lambda}$, it will violate unitarity as $x \to 0$. Indeed, even after the NLL resummation, the expected power, $\lambda \simeq 0.3$, is rather large. Thus, we first discuss absorption effects which tame the violation of unitarity. The upper limit of the small x behaviour of the parton distributions $a = g, q$ is given by the extrapolation

$$xa(x, q^2) = \left(\frac{x_0}{x}\right)^{0.3} x_0 a(x_0, q^2) \tag{1}$$

below $x_0 = 0.001$. The distributions are reliably determined from global parton analyses at $x > x_0$.

On the other hand, it is reasonable to expect that at $Q \lesssim Q_0 \sim 1$ GeV the behaviour will reflect that of hadron-hadron interactions: $\lambda = 0.08$ [16]. Most likely the lower value of λ is explained by
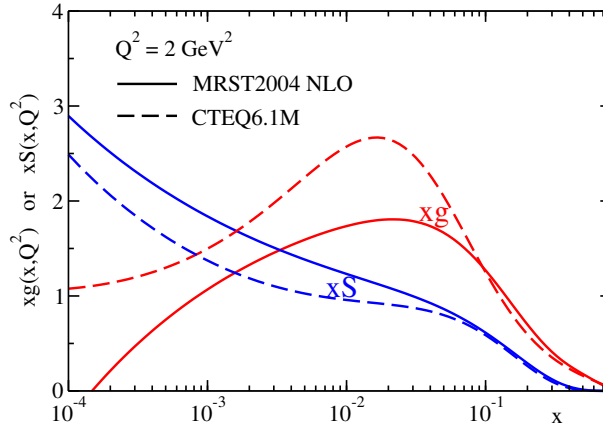
Fig. 2: The behaviour of the gluon and sea quark distributions at $Q^2 = 2$ GeV^2 found in the CTEQ6.1M [17] and MRST2004 NLO [18] global analyses. The valence-like behaviour of the gluon is evident.

absorptive/screening effects in hadron-hadron collisions. So, for extrapolation down to $x \sim 10^{-7} - 10^{-6}$ we may regard $\lambda = 0.08$ as a lower limit since, in DIS, we expect smaller absorptive effects than those in hadron-hadron interactions.

However, present global analyses, which do not allow for absorption effects, reveal that at $Q \sim 1 - 1.5$ GeV and low x, the sea quarks have a Pomeron-like behaviour, $xq \sim x^{-0.2}$, whereas the gluon distribution has a valence-like behaviour, $xg \sim \sqrt{x}$. This different behaviour is evident from Fig. 2, which shows the behaviour of the gluon and sea quark distributions, $xS = 2x(\bar{u} + \bar{d} + \bar{s})$ for $Q^2 = 2$ GeV^2. Such a result looks strange from the Regge viewpoint where the same vacuum singularity (Pomeron) should drive both the sea quarks and the gluons since the same power is expected for sea quarks and gluons, $\lambda_g = \lambda_q$.

This difference demonstrates that the actual situation is even more complicated. It is worth noting that a simultaneous analysis of inclusive and diffractive DIS data indicates that, after accounting for screening effects and allowing for some power corrections, it may be possible to describe the HERA data with $\lambda_g = \lambda_q = 0$ [19]. The absorptive effects, estimated from fitting the diffractive DIS data, enlarge the input gluon distribution at low x.

It may initially seem strange that accounting for absorptive effects gives a *larger* gluon density[2] at low x and Q^2. The point is that the only way to describe the data, *which are sensitive to absorptive effects*, within the framework of DGLAP evolution without absorption, is to choose a very low 'input' gluon density in order to *mimic* the screening corrections 'hidden' in the data. Indeed, there is a tendency for the gluon distribution to even become negative at low x and Q^2. On the other hand, allowing for absorption during DGLAP evolution (with the help of the Gribov-Levin-Ryskin (GLR) and Mueller-Qiu (MQ), GLRMQ, equations [22, 23]) the same data may be described with a larger and definitely positive input gluon density at $Q = Q_0$.

2.3 Estimates of absorptive effects: GLRMQ to BK

The saturation of parton densities ($\lambda = 0$) may be obtained using the Balitski-Kovchegov (BK) [24, 25] equation, based on the BFKL equation, as well as the aforementioned GLRMQ equations. The latter equation is based on DGLAP evolution. These equations sum the set of fan diagrams which describe the rescattering of intermediate partons on the target nucleon. The screening caused by these rescatterings prohibits the power growth of the parton densities.

---

[2]The same result was obtained in Ref. [20, 21] – note, however, it was based on LO evolution and the large NLO correction to P_{qg} will change the q, g relationship.

The GLR equation for the gluon may be written symbolically as

$$\frac{\partial xg}{\partial \ln Q^2} = P_{gg} \otimes g + P_{gq} \otimes q - \frac{81\alpha_s^2}{16R^2Q^2} \int \frac{dy}{y}[y\,g(y,Q^2)]^2 \,. \tag{2}$$

The nonlinear shadowing term, $\propto -[g]^2$, arises from perturbative QCD diagrams which couple four gluons to two gluons so that two gluon ladders recombine into a single gluon ladder. The minus sign occurs because the scattering amplitude corresponding to a gluon ladder is predominantly imaginary. The parameter R is a measure of the transverse area πR^2 where the gluon density is sufficiently dense for recombination to occur.

The BK equation is an improved version of the GLR equation. It accounts for the more precise triple-pomeron vertex (first calculated in Ref. [26–28]) and can be used for the non-forward amplitude. The GLR equation was in momentum space, whereas the BK equation is written in coordinate space in terms of the dipole scattering amplitude $N(\mathbf{x},\mathbf{y},Y) \equiv N_{\mathbf{xy}}(Y)$. Here $\mathbf{x}$ and $\mathbf{y}$ are the transverse coordinates of the two t-channel gluons which form the colour-singlet dipole and $Y = \ln(1/x)$ is the rapidity. The BK equation reads

$$\frac{\partial N_{\mathbf{xy}}}{\partial Y} = \frac{\alpha_s N_c}{\pi} \int \frac{d^2\mathbf{z}}{2\pi} \frac{(\mathbf{x}-\mathbf{y})^2}{(\mathbf{x}-\mathbf{z})^2(\mathbf{y}-\mathbf{z})^2} \left\{ N_{\mathbf{xz}} + N_{\mathbf{yz}} - N_{\mathbf{xy}} - N_{\mathbf{xz}}\,N_{\mathbf{yz}} \right\} \,. \tag{3}$$

For small dipole densities, N, the quadratic term in the brackets may be neglected and Eq. (3) reproduces the conventional BFKL equation. However for large N, that is $N \to 1$, the right-hand side of Eq. (3) vanishes and we reach saturation when $N = 1$. The equation sums up the set of fan diagrams where at small Y the target emits any number of pomerons (i.e. linear BFKL amplitudes) while at large Y we have only one BFKL dipole.

Starting from the same initial conditions, the solution of the BK equation gives *fewer* small-x partons than that predicted by its *parent* linear BFKL/CCFM equation[3].

In principle, it would appear more appropriate to use the BFKL-based BK equation to describe the parton densities at low x. Unfortunately, however, the BK equation is only a model. It cannot be used for numerical predictions. We discuss the reasons below.

2.4 Status of the BK equation

The Balitski-Kovchegov (BK) equation [24,25] is an attempt to describe saturation phenomena. However it is just a 'toy model' and cannot, at present, be used to reliably estimate absorptive effects at small x. The reasons are as follows:

- The BK equation is based on the LO BFKL/CCFM equation. We know that the NLL corrections are large. We need to know the NLL corrections not only for the linear part of the evolution, but also for the nonlinear term.
- Even neglecting the NLL corrections, we need to match the solution to a boundary condition at rather low Q^2. This boundary condition is not theoretically known.
- It sums a limited set of diagrams. The selection of diagrams (the fan graphs) was justified in the region where absorptive effects are relatively small. When these corrections become important, as in the saturation region, one has to allow for many other graphs whose contributions become comparable to the fan diagram contributions[4].

---

[3] Analogously, starting from the same input (and not fitting the input to the data) the GLR equation gives fewer small-x partons than that predicted by the parent linear DGLAP equation.

[4] Unfortunately the problem of summing all relevant diagrams has not been solved, even in the simpler case of Reggeon field theory.

   – To solve the BK equation we need an initial condition at fixed x and all Q^2. These conditions are not well enough known. In particular, the maximum (saturation) value of the gluon density depends on the radius: $xg(x, q^2) \propto R^2 q^2$. At the moment, the radius R is a free parameter. It may be small — the so-called 'hot spot' scenario. Moreover, we should account for the possibility of dissociation of the target proton[5]. The contribution coming from the dissociation is expected to have a smaller R.

2.5 Relevance to, and of, the LHC

How do the uncertainties at low x affect the predictions for the LHC? Fortunately for inclusive production of possible massive new particles with $M \gtrsim 100$ GeV, the partons are sampled at x values and scales M reliably determined from NLO and NNLO global analyses. For illustration, we discuss W production which has been studied in detail [29–31]. Central W production ($y_W = 0$) at the LHC samples partons at $x = M_W/\sqrt{s} = 0.006$. However to predict the total cross section, σ_W, we need to integrate over rapidity, important for $|y_W| \lesssim 4$ so that σ_W has some sensitivity to partons as low as $x \sim 10^{-4}$. The total uncertainty on the NNLO prediction of σ_W has been estimated to be $\pm 4\%$ [29]. Therefore W production at the LHC can serve as a good luminosity monitor. To reduce the uncertainty in the prediction of σ_W will require a better theoretical understanding of low x partons.

    Of course, if the new particles are sufficiently massive, $M \gtrsim 1$ TeV, and produced by gluon fusion, then the uncertainties due to the PDFs will be larger. However, there are situations where the scale is considerably lower such as exclusive double-diffractive Higgs production which depends on the unintegrated gluon at $Q^2 \approx 5$ GeV^2 with $x \sim M_H/\sqrt{s} \sim 0.01$. The absorptive effects are also expected to be small here.

    Turning the discussion around, is it possible for the LHC experiments to determine the behaviour of partons in the x region below 10^{-4} at low scales? One possibility is $\mu^+ \mu^-$ Drell-Yan production in which events are observed with the $\mu^+ \mu^-$ invariant mass as low as possible and the rapidity as large as possible. For example, for $M_{\mu\mu} = 4$ GeV and $y_{\mu\mu} = 3$, we sample quarks at $x = 1.4 \times 10^{-5}$. This process predominantly samples the sea quark distributions. To study the small x behaviour of the gluon at low scales we may consider χ_c production, or prompt photon production driven by the subprocess $gq \rightarrow \gamma q$.

    In practice, rather than χ_c, it may be better to study $pp \rightarrow J/\psi\, X$ as a function of $y_{J/\psi}$. This process is also sensitive to the gluon distribution through the subprocesses $gg \rightarrow J/\psi\, g$, $gg \rightarrow \chi \rightarrow J/\psi\, \gamma$. There are also contributions from the subprocesses $gg \rightarrow b\bar{b}$ with $b \rightarrow J/\psi$, and $q\bar{q} \rightarrow J/\psi$. The analysis of such data will be considerably helped by the detailed observations of prompt J/ψ and J/ψ from b in central production at the Tevatron [32]. In fact, the first ever NLO global parton analysis [33] used J/ψ data as a function of rapidity to constrain the gluon distribution.

    The LHCb detector covers the rapidity region of $2 < \eta < 5$ [34], and may be able to perform some of the above measurements. There is another possibility. Since LHCb will operate at a luminosity of 2×10^{32} cm^{-2}s^{-1}, there will usually be a single collision per bunch crossing and thus practically no 'pile-up' problems. Installing a forward detector at LHCb would offer the possibility of observing asymmetric events with one very large rapidity gap to probe the region of $x_{I\!P} \leq 10^{-5}$.

3 Including nonlinear terms in gluon evolution: the GLRMQ and BK approaches

3.1 GLRMQ approach[6]

The DGLAP [1–4] evolution equations describe the scale evolution of the parton distribution functions (PDFs) well in the region of large interaction scale, $Q^2 \gtrsim 4$ GeV^2 [17, 35, 36]. However, toward small

---

[5] We know that these channels provide more than $30 - 40\%$ of F_2^D measured at HERA.

[6] Authors: K.J. Eskola and V.J. Kolhinen

values of x and Q^2, the gluon recombination terms start to play an increasingly important role. The inclusion of correction terms which arise from fusion of two gluon ladders leads to nonlinear power corrections to the DGLAP evolution equations. The first of these nonlinear corrections are the GLRMQ terms.
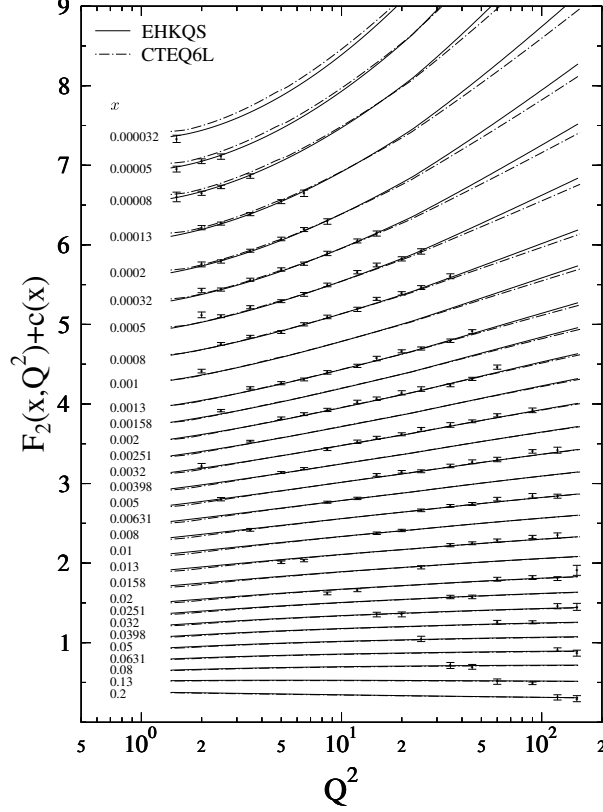

Fig. 3: Calculated $F_2(x, Q^2)$ values compared with the H1 data.

With the GLRMQ corrections, the gluon evolution equation becomes

$$\frac{\partial xg(x, Q^2)}{\partial \ln Q^2} = \frac{\partial xg(x, Q^2)}{\partial \ln Q^2}\bigg|_{\text{DGLAP}} - \frac{9\pi}{2}\frac{\alpha_s^2}{Q^2}\int_x^1 \frac{dy}{y}y^2 G^{(2)}(y, Q^2). \tag{4}$$

We model the two-gluon density in the latter term on the right-hand side as

$$x^2 G^{(2)}(x, Q^2) = \frac{1}{\pi R^2}[xg(x, Q^2)]^2, \tag{5}$$

where $R = 1$ fm is the radius of the proton (we comment further on this later). The corrections to the sea quark distributions are

$$\frac{\partial xq(x, Q^2)}{\partial \ln Q^2} \approx \frac{\partial xq(x, Q^2)}{\partial \ln Q^2}\bigg|_{\text{DGLAP}} - \frac{3\pi}{20}\frac{\alpha_s^2}{Q^2}x^2 G^{(2)}(x, Q^2).$$

We have assumed that the higher-twist gluon term, G_{HT} [23], is negligible.

Since these correction terms are negative, they slow down the evolution of the PDFs. Due to the $1/Q^2$ dependence, they also die out in the evolution so that at large scales Eqs. (4) and (6) relax into the linear DGLAP equations.
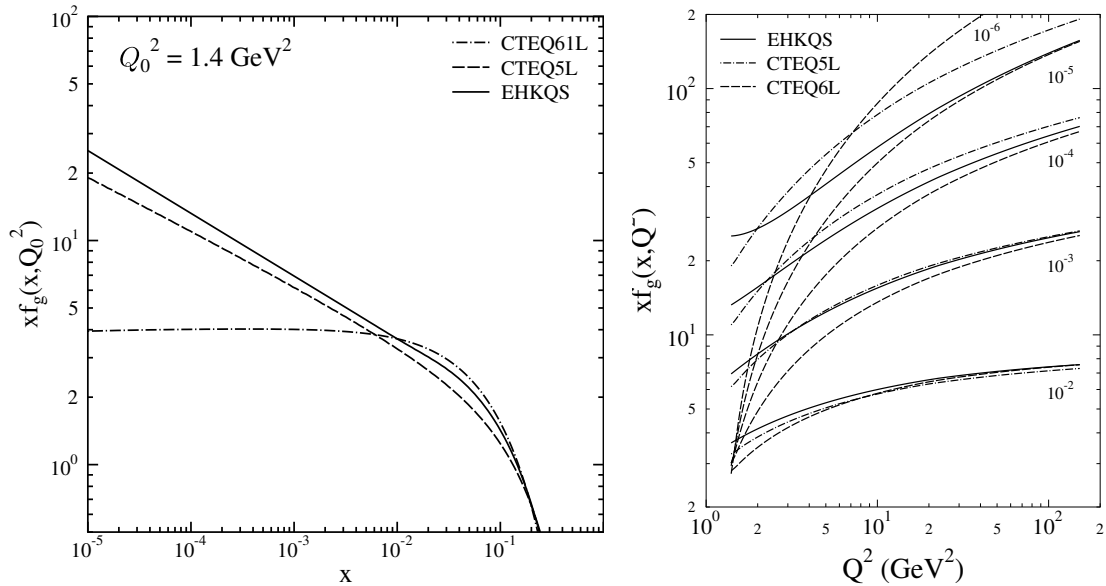
Fig. 4: Left: initial gluon distributions at $Q_0^2 = 1.4\,\mathrm{GeV}^2$. Right: evolution of gluon distributions for several fixed values of x shows that the effect of the nonlinear terms vanishes as Q^2 increases.

In order to study the interplay between the nonlinear corrections and the initial PDFs and observe the nonlinear effects in fits to the DIS data, in Ref. [37] we compared the structure function $F_2(x, Q^2) = \sum_q e_q^2 [xq(x,Q^2) + x\bar{q}(x,Q^2)]$, calculated with the nonlinearly-evolved PDFs, to the HERA H1 data [38]. As reference distributions we used the CTEQ5L and CTEQ6L PDF sets at large scales. We chose these sets because the CTEQ collaboration uses only the large scale, $Q^2 > 4\,\mathrm{GeV}^2$, data in their fits, thus avoiding some of the possible nonlinear effects appearing in the small x, $Q^2 < 4\,\mathrm{GeV}^2$ region in their initial distributions.

At small x, sea quarks dominate F_2 and the gluon distribution dictates its scale evolution. At leading order (LO), the DGLAP contribution can be approximated as [39]:

$$\partial F_2(x, Q^2)/\partial \ln Q^2 \approx (10\alpha_s/27\pi)xg(2x, Q^2) \ .$$

Larger $xg(x, Q^2)$ values correspond to faster $F_2(x, Q^2)$ evolution. The scale evolution of $F_2(x, Q^2)$ at small x computed with CTEQ5L is too fast due to a large small-x small-Q^2 gluon distribution. The newer CTEQ6L set has much smaller gluon distribution in this region (see Fig. 4 (left)), giving a slower evolution and hence a good fit to the H1 data.

Our goal in Ref. [37] was to determine whether the good fit to the data could be maintained using the GLRMQ-corrected DGLAP scale evolution together with initial scale PDFs differing from CTEQ6L. We constructed a new set of PDFs using the CTEQ5L and CTEQ6L distributions piecewise as baselines at scales $Q^2 \sim 3 - 10\,\mathrm{GeV}^2$ where the linear terms dominate the evolution and evolved them nonlinearly to lower Q^2. We then interpolated between the sets in x and assumed a power-like dependence at small-x for gluons and sea quarks. These initial PDF candidates were then evolved to higher scales and compared to the data. This iterative procedure was repeated until a sufficiently good fit to the data was found.

As a result, we obtained a new set of initial PDFs[7], called EHKQS, which, when evolved using the nonlinear DGLAP+GLRMQ evolution equations, produced an equally good or even better fit to the H1 data relative to CTEQ6L, shown in Fig. 3. At $Q^2 \sim 1.4\,\mathrm{GeV}^2$ and $x \sim 10^{-5}$, a good fit to the HERA data requires the nonlinear evolution to be compensated by a larger gluon distribution than obtained with

---

[7]In fact, we produced three new sets of initial distributions, differing by the charm quark mass and parton distribution at the initial scale, see Ref. [37] for more details. All sets produced equally good fits to the HERA data.

DGLAP alone. The enhancement is a factor of ~ 6 relative to CTEQ6L, as shown in Fig. 4 (left). The Q^2 dependence of EHKQS is compared to CTEQ6L and CTEQ5L in Fig. 4 (right) for several different values of x.

We used $R = 1$ fm as the free proton radius in the two-gluon density term. We did not repeat the calculations with different R but, depending on the transverse matter density of the free proton, some $\sim 20\%$ uncertainty in R can be expected. Since the nonlinear contributions decrease as R increases, a larger R would lead to reduced enhancement of the small x gluons below $Q^2 \sim 10$ GeV^2. Thus, minimizing the χ^2 of the fit with respect to R is a future task.

3.2 BK approach[8]

A theoretical framework capable of describing the QCD evolution of parton densities taking gluon rescattering (corresponding to nonlinear effects) into account is the Balitsky-Kovchegov (BK) equation [24, 25, 40–42]. The equation, based on the BFKL approach [6, 7, 43], may be used to determine the unintegrated gluon density. The BK equation resums the BFKL pomeron fan diagrams with the triple pomeron vertex derived in the high energy limit of QCD. In the doubly logarithmic limit, the BK equation reduces [25] to the collinear Gribov-Levin-Ryskin (GLR) equation [22]. It is the non-collinear limit, however, which gives the dominant contribution to the triple pomeron vertex [44, 45]. We conclude that GLR approach misses an essential part of the nonlinear gluon dynamics.

The solution to the BK equation, constrained by the low-x HERA data will be used to extrapolate the parton densities to the LHC kinematical domain. Extrapolation is necessary as the LHC may probe very low values of x, down to 10^{-7} for $M = 10$ GeV and $\eta \sim 9$, where unitarity corrections may be important even at relatively large scales of a few GeV^2. Last but not least, unitarity corrections may also break k_T factorization. We will also discuss which processes may be affected.

This section is organized as follows. First we give a brief description of the formalism used to determine the gluon evolution. Within this formalism, we fit the HERA charm structure function, F_2^c, data, the most relevant inclusive measurement directly sensitive to the gluon density. Using further assumptions about the sea quarks, F_2 can also be described well. The resulting gluon density is then used to compute heavy quark production and to investigate the nonlinear effects. First we estimate $b\bar{b}$ production at CDF and D0. Then, cross sections for heavy quark production at various LHC experiments are estimated, tracing the impact of the unitarity corrections. Finally, conclusions are given.

The standard framework to determine parton evolution is the collinear DGLAP formalism. It works rather well for inclusive quantities but, for more exclusive processes, the k_T-factorization scheme is more appropriate because both the longitudinal and transverse components of the gluon momenta are considered. In this framework, the process-independent quantity is the unintegrated gluon distribution, connected to the process-dependent hard matrix element via the k_T-factorization theorem. Linear evolution of the unintegrated gluon distribution may be described by one of the small x evolution equations using the k_T-factorization scheme, the BFKL and CCFM [46–49] equations. These equations are based on resummation of large logarithmic pQCD corrections, $\alpha_s^n \ln^m(1/x)$, and are equivalent at the leading logarithmic level.

The very small x kinematic region is also the regime where the growth of the gluon density must be tamed in order to preserve unitarity. Recently, a successful description of unitarity corrections to DIS was derived within the color dipole formulation of QCD. This is the Balitsky-Kovchegov (BK) equation which describes the BFKL evolution of the gluon in a large target, including a nonlinear term corresponding to gluon recombination at high density.

In our analysis, we determine the unintegrated gluon distribution from the BK equation unified with the DGLAP equation following KMS (Kwieciński, Martin and Staśto) [50–53]. We use the abbreviation KKMS (Kutak, Kwieciński, Martin and Staśto) [52, 53] for the unified nonlinear equation.

---

[8]Authors: H. Jung, K. Kutak, K. Peters, L. Motyka

The linear part of this equation is given by the BFKL kernel with subleading $\ln(1/x)$ corrections, supplemented by the non-singular parts of the DGLAP splitting functions. Thus resummation of both the leading $\ln Q^2$ and $\ln(1/x)$ terms are achieved. The subleading terms in $\ln(1/x)$ are approximated by the so-called consistency constraint and the running coupling constant. The nonlinear part is taken directly from the BK equation, ensuring that the unitarity constraints are preserved. One expects that this framework provides a more reliable description of the gluon evolution at extremely small x, where $\ln(1/x) \gg 1$ and the unitarity corrections are important, than does DGLAP.

We give a short review of the KKMS equation, starting from the impact parameter dependent BK equation. The equation for the unintegrated gluon density, $h(x, k^2, b)$, at impact parameter b from the center of the target, becomes

$$\frac{\partial h(x, k^2, b)}{\partial \ln 1/x} = \frac{\alpha_s N_c}{\pi} k^2 \int_{k_0^2} \frac{dk'^2}{k'^2} \left\{ \frac{h\left(x, k'^2, b\right) - h\left(x, k^2, b\right)}{|k'^2 - k^2|} + \frac{h\left(x, k^2, b\right)}{[4k'^4 + k^4]^{\frac{1}{2}}} \right\}$$
$$-\pi\alpha_s \left(1 - k^2 ddk^2\right)^2 k^2 \left[\int_{k^2}^{\infty} \frac{dk'^2}{k'^4} \ln\left(\frac{k'^2}{k^2}\right) h(x, k'^2, b) \right]^2, \tag{6}$$

the BFKL equation at LLx accuracy, extended by the negative recombination term. The (dimensionless) unintegrated gluon distribution is obtained from $h(x, k^2, b)$ by integration over b,

$$f(x, k^2) = \int d^2b \, h(x, k^2, b). \tag{7}$$

A comment about the impact parameter treatment is in order. In Eq. (7), we assume that the evolution is local in b. However, the complete BK equation results in some diffusion in the impact parameter plane. This diffusion effect may be neglected if the target is much larger than the inverse of the saturation scale. In this scheme, the impact parameter dependence enters through the initial condition at large x_0, $h(x_0, k^2, b) = f(x_0, k^2)S(b)$ where $f(x_0, k^2)$ is the unintegrated gluon distribution. Note that, due to nonlinearities, the b dependence of $h(x, k^2, b)$ does not factorize from x and k at low x.

The input profile function is assumed to be Gaussian, $S(b) = \exp(-b^2/R^2)/\pi R^2$, where R^2 corresponds to the square of the average nucleon radius. Since the size of the target, R, sets the magnitude of the initial parton density in the impact parameter plane, $h(x_0, k^2, b)$, the unitarity corrections depend on R. At smaller R, gluons are more densely packed in the target and the nonlinear effects are stronger.

References [52, 53] proposed to combine Eq. (6) with the unified BFKL-DGLAP framework developed in Ref. [50]. In this scheme, the (linear) BFKL part is modified by the consistency constraint [54, 55], resulting in the resummation of most of the subleading corrections in $\ln(1/x)$ which arise from imposing energy-momentum conservation on the BFKL kernel [56–59]. In addition, we assume that the strong coupling constant runs with scale k^2, another source of important NLLx corrections. Finally, the non-singular part of the leading order DGLAP splitting function and quark singlet distribution were included in the x evolution. The final improved nonlinear equation for the unintegrated gluon density is

$$h(x, k^2, b) = \tilde{h}^{(0)}(x, k^2, b) +$$
$$+ \frac{\alpha_s(k^2)N_c}{\pi} k^2 \int_x^1 \frac{dz}{z} \int_{k_0^2} \frac{dk'^2}{k'^2} \left\{ \frac{h(\frac{x}{z}, k'^2, b)\,\Theta(\frac{k^2}{z} - k'^2) - h(\frac{x}{z}, k^2, b)}{|k'^2 - k^2|} + \frac{h(\frac{x}{z}, k^2, b)}{|4k'^4 + k^4|^{\frac{1}{2}}} \right\} +$$
$$+ \frac{\alpha_s(k^2)}{2\pi} \int_x^1 dz \left[\left(P_{gg}(z) - \frac{2N_c}{z}\right) \int_{k_0^2}^{k^2} \frac{dk'^2}{k'^2} h(\frac{x}{z}, k'^2, b) + P_{gq}(z)\Sigma\left(\frac{x}{z}, k'^2, b\right) \right] +$$
$$- \pi \left(1 - k^2 \frac{d}{dk^2}\right)^2 k^2 \int_x^1 \frac{dz}{z} \left[\int_{k^2}^{\infty} \frac{dk'^2}{k'^4} \alpha_s(k'^2) \ln\left(\frac{k'^2}{k^2}\right) h(z, k'^2, b) \right]^2. \tag{8}$$

The second line of the equation corresponds to the BFKL evolution. The theta function, $\Theta(\frac{k^2}{z} - k'^2)$, reflects the consistency constraint that generates the dominant part of the subleading BFKL corrections.
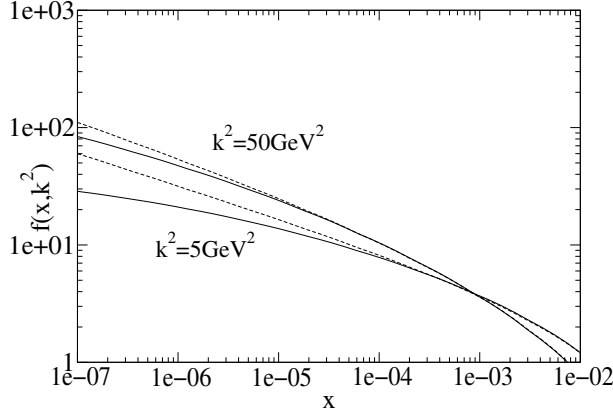
Fig. 5: The unintegrated gluon distribution obtained from Eq. (8) as a function of x for different values of k_T^2. The solid lines correspond to the solution of the nonlinear equation with $R = 2.8 \, \text{GeV}^{-1}$ while the dashed lines correspond to the linear part.

The third line corresponds to the DGLAP effects generated by the part of the splitting function, $P_{gg}(z)$, that is not singular in the limit $z \to 0$ and also by the quarks where $\Sigma(x, k^2, b^2)$ corresponds to the impact-parameter dependent singlet quark distribution. The nonlinear screening contribution following from the BK equation is given in the last term. The inhomogeneous contribution, defined in terms of the integrated gluon distribution, carries information about the transverse profile of the proton,

$$\tilde{h}^{(0)}(x, k^2, b) = \frac{\alpha_s(k^2)}{2\pi} \, S(b) \int_x^1 dz P_{gg}(z) \frac{x}{z} g\left(\frac{x}{z}, k_0^2\right) \; , \qquad (9)$$

at $k_0^2 = 1 \, \text{GeV}^2$. The initial integrated density at k_0^2 is parameterized as

$$xg(x, k_0^2) = N(1 - x)^\rho \qquad (10)$$

where $\rho = 2.5$. The size of the dense gluon system inside the proton is assumed to be $R = 2.8 \, \text{GeV}^{-1}$, in accord with the diffractive slope, $B_d \simeq 4 \, \text{GeV}^{-2}$, of the elastic J/ψ photoproduction cross section at HERA. In this process, the impact parameter profile of the proton defines the t dependence of the elastic cross section, $B_d \simeq R^2/2$, by Fourier transform. In the 'hot-spot' scenario, the radius can be smaller, $R = 1.5 \, \text{GeV}^{-1}$. We also use the hot spot value to compare with measurements and make predictions for the LHC.

Equation (8) was solved numerically both in the linear approximation and in full. The method for solving Eq. (8) was developed in Refs. [50, 52]. In Fig. 5, the effects of linear and nonlinear evolution on the unintegrated gluon distribution are given as a function of x for $k^2 = 5$ and $50 \, \text{GeV}^2$. Nonlinear evolution leads to sizeable suppression at the smallest x values. While the nonlinear effects are small in the HERA x range, they may be important at the LHC. In the following sections, we address the importance of these nonlinear effects.

The initial distribution in Eq. (10) was obtained by fitting the HERA F_2^c measurements [60, 61] using the Monte Carlo CASCADE [62, 63] for evolution and convolution with the off-shell matrix elements. We find χ^2 per degree of freedom of 0.46 (1.17) for H1 (ZEUS). The fits were repeated both with the standard KMS evolution without the nonlinear contribution and with extended KMS evolution including the nonlinear part. The predicted F_2^c is equivalent for both linear and nonlinear evolution, independent of R. Thus nonlinear evolution is only a small effect at HERA, even in the hot-spot scenario with $R = 1.5$ GeV^{-1}.

In Fig. 6(a) we compare the measured F_2^c [61] to our prediction at $Q^2 = 4 \, \text{GeV}^2$. We have determined our initial distribution from F_2^c since it is the only inclusive measurement at HERA directly
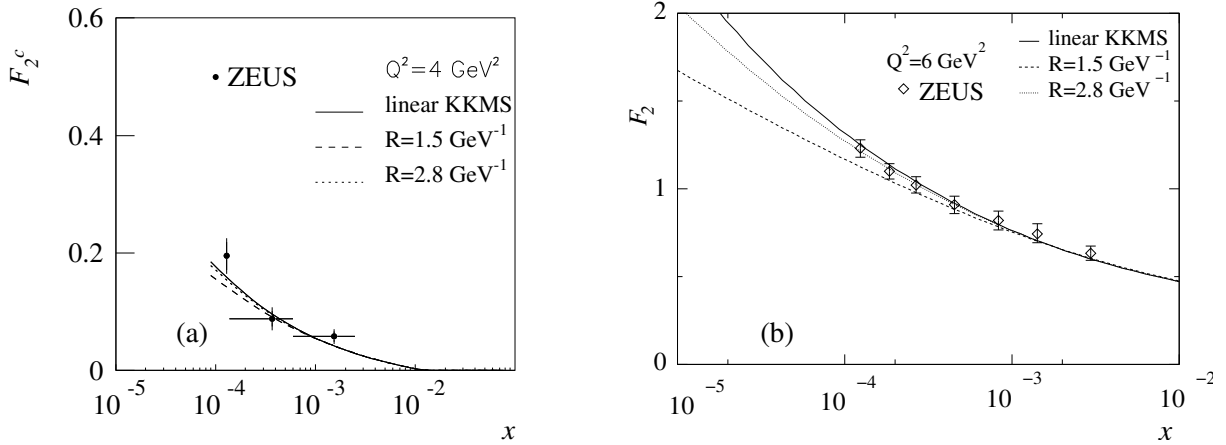
Fig. 6: The charm structure function, F_2^c, [61] at $Q^2 = 4$ GeV^2 (a) and F_2 [64] at $Q^2 = 6$ GeV^2 (b) obtained for KKMS evolution with different values of R.
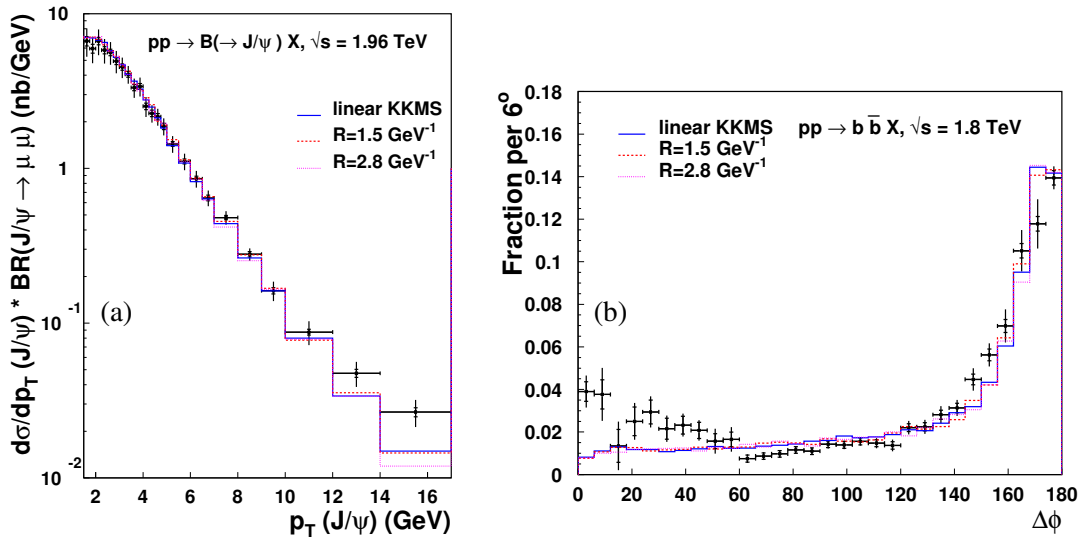
Fig. 7: Bottom production, measured by CDF, is compared to predictions using CASCADE with linear and non-linear KKMS evolution, including two values of R. (a) The p_T distribution of B meson decays to J/ψ. (b) The azimuthal angle, $\Delta\phi$, distribution of $b\bar{b}$ pair production smeared by the experimental resolution.

sensitive to the gluon distribution. However, we can also describe F_2 [64] by making further assumptions about the sea quark distribution, following the KMS approach. The agreement with the data, shown in Fig. 6(b), is also quite good. There is only a small effect for $Q^2 > 5$ GeV^2, even in the hot-spot scenario with $R = 1.5$ GeV^{-1}.

Next, this constrained gluon density was used to calculate $gg \to b\bar{b}$ production at the Tevatron as a cross check of the fit and the evolution formalism. We use $m_b = 4.75$ GeV and a renormalization scale in α_s of $Q^2 = 4m_b^2 + p_T^2$. The predicted cross section was then compared to both CDF [65, 66] and D0 [67] measurements. The predictions agree well with the data.

In Fig. 7(a) the cross section for B decays to J/ψ is shown as a function the J/ψ p_T [65, 66]. The KKMS gluon density fits the data well in all three scenarios with deviations only appearing for $p_T > 12$ GeV. It is interesting to note that the approach described here gives even better agreement than the NLO collinear approach [68].

In Fig. 7(b), the azimuthal angle distribution between the b and $\bar{b}$ quarks, $\Delta\phi$, is given. The $\Delta\phi$ and $b\bar{b}$ p_T distributions are correlated since $\Delta\phi < 180°$ corresponds to higher pair p_T. Since the k_T-factorization formula allows the incoming gluons to have sizable transverse momenta, the calculated $\Delta\phi$ distribution agrees very well with the data for $\Delta\phi > 60°$ with only smearing due to the experimental resolution. The enhancement of the data relative to the calculations at low $\Delta\phi$ requires further study.

Both plots compare linear (solid histograms) and nonlinear KKMS evolution (dotted and dashed histograms) for $R = 1.5$ GeV^{-1} and 2.8 GeV^{-1} respectively. The nonlinear part of the evolution also has no impact in this kinematic region.

4 Phenomenological applications: heavy quark production at the LHC

4.1 GLRMQ approach[9]

Since the HERA F_2 data can be described by both linear DGLAP and nonlinear DGLAP+GLRMQ evolution, as shown in Fig. 3 of Section 3.1, additional independent probes are needed. Here, we discuss how charm quark production in pp collisions could probe the gluon enhancement predicted in Section 3.1 and described in detail in Ref. [20, 21]. Charm production is an ideal choice since the charm mass is low and its production is dominated by gluons. Assuming factorization, the inclusive differential charm cross section is

$$d\sigma_{pp\to c\bar{c}X}(Q^2, \sqrt{s}) = \sum_{i,j,k=q,\bar{q},g} f_i(x_1, Q^2) \otimes f_j(x_2, Q^2) \otimes d\hat{\sigma}_{ij\to c\bar{c}\{k\}}(Q^2, x_1, x_2) \tag{11}$$

where $\hat{\sigma}_{ij\to c\bar{c}\{k\}}(Q^2, x_1, x_2)$ are the perturbatively calculable partonic cross sections for charm production at scales $Q^2 \sim m_T^2 \gg \Lambda_{\text{QCD}}^2$, x_1 and x_2 are the parton momentum fractions and $f_i(x, Q^2)$ are the proton parton densities. We assume that the renormalization and factorization scales are equal. Only the leading order gg and $q\bar{q}$ channels are considered here.

The values of the charm quark mass and scale used in the calculations are chosen to give good agreement with the total cross section data at NLO: $m = 1.2$ GeV and $Q^2 = 4m^2$ for standard DGLAP-evolved NLO PDFs such as CTEQ6M [69] and MRST [70]. Nearly equivalent agreement may be obtained with $m = 1.3$ GeV and $Q^2 = m^2$ [71, 72]. Both choices assure that the PDFs are evaluated above the minimum scales. While scales proportional to m are used in the total cross section, inclusive calculations of distributions also depend on the transverse momentum scale, p_T, so that $m_T = \sqrt{m^2 + p_T^2}$ is used instead [73].

To illustrate the effects of the nonlinear EHKQS distributions [37] of Section 3.1 on charm production at the LHC, we show

$$R(y) \equiv \frac{d\sigma(\text{EHKQS})/dy}{d\sigma(\text{CTEQ61L})/dy} \quad \text{and} \quad R(p_T) \equiv \frac{d\sigma(\text{EHKQS})/dp_T}{d\sigma(\text{CTEQ61L})/dp_T} \tag{12}$$

in Fig. 8 where y is the charm quark rapidity. The results are calculated for the maximum LHC pp, pPb and Pb+Pb energies, $\sqrt{S} = 14$ (solid), 8.8 (dashed) and 5.5 (dot-dashed) TeV respectively. The results for $m = 1.2$ GeV and $Q^2 = 4m_T^2$ are on the left-hand side while those with $m = 1.3$ GeV and $Q^2 = m_T^2$ are on the right-hand side.

The change in the slope of $R(y)$ occurs when one x drops below the minimum value of the EHKQS set where further nonlinearities become important, $x_{\min}^{\text{EHKQS}} = 10^{-5}$, and enters the unconstrained x region. The minimum x of CTEQ61L is lower, $x_{\min}^{\text{CTEQ61L}} = 10^{-6}$. While the EHKQS gluon distribution is fixed at its minimum for $x < x_{\min}^{\text{EHKQS}}$, the CTEQ61L distribution continues to change until $x_{\min}^{\text{CTEQ61L}}$.

---

[9]Author: R. Vogt
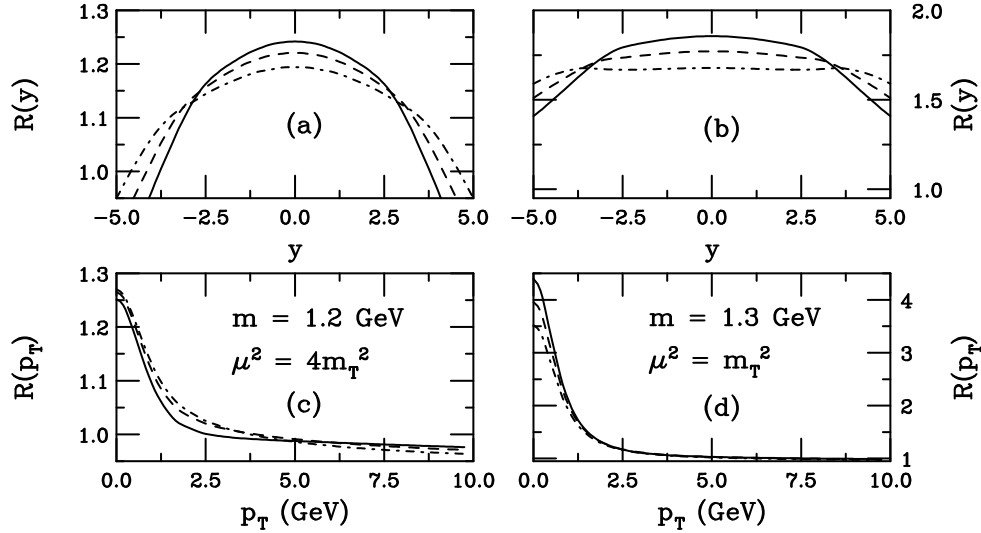
Fig. 8: We present $R(y)$, (a) and (c), and $R(p_T)$, (b) and (d), in pp collisions at $\sqrt{S} = 14$ (solid), 8.8 (dashed) and 5.5 (dot-dashed) TeV. The left-hand side shows $m = 1.2$ GeV and $Q^2 = 4m_T^2$, the right-hand side $m = 1.3$ GeV and $Q^2 = m_T^2$.

In inclusive kinematics with an identified charm quark and fixed $x_T = 2m_T/\sqrt{S}$, the unconstrained x-region contributes to charm production in the region

$$y_l \equiv \ln\left(1/x_T - \sqrt{1/x_T^2 - 1/x_{\min}}\right) \leq |y| \leq \ln\left(1/x_T + \sqrt{1/x_T^2 - 1/x_{\min}}\right) . \qquad (13)$$

The upper limit is close to the phase space boundary. Expanding the lower limit, y_l, in powers of $x_T^2/x_{\min} \ll 1$, $y_l \approx \ln[m_T/(x_{\min}\sqrt{S})] \geq \ln[m/(x_{\min}\sqrt{S})]$. If $m = 1.2$ GeV, the small x region contributes to charm production at $|y| \geq y_l = 2.2$, 2.6 and 3.1 for $\sqrt{S} = 14$, 8.8 and 5.5 TeV, respectively. The rather sharp turnover in $R(y)$ indicates where the $x < 10^{-5}$ region begins to contribute. For $|y| > y_l$ and $Q^2 > 4$ GeV^2, as x decreases, the CTEQ61L gluon distribution increases considerably above that of the EHKQS distribution. Thus $R(y) < 1$ at large rapidities when $Q^2 = 4m_T^2$. At midrapidity $R(y)$ is insensitive to the EHKQS extrapolation region, $x < x_{\min}^{\text{EHKQS}}$. Since $R(y)$ is integrated over p_T, it not only reflects the enhancement at $m_T = m$ because $Q^2 \propto m_T^2$ and the p_T distribution peaks around $p_T \approx 1$ GeV. When $Q^2 = m_T^2$, the ratios are broad because the CTEQ61L gluon distribution is relatively flat as a function of x for $Q^2 \sim 2 - 3$ GeV^2. The enhancement decreases and broadens with decreasing energy.

Since the rapidity distributions are rather flat, there are still important contributions to the p_T distributions from the extrapolation region, up to $\sim 30\%$ at $\sqrt{S} = 14$ TeV for $m = 1.2$ GeV and $Q^2 = 4m^2$. Thus the sensitivity of $R(p_T)$ to the unconstrained region should be kept in mind. At the largest $\sqrt{S}$, the contribution from the $x < 10^{-5}$ region is greatest and if $Q^2 \geq 4m^2$, $xg^{\text{CTEQ61L}}(x, Q^2) > xg^{\text{EHKQS}}(x, Q^2)$. Because the contribution from the region $x < 10^{-5}$ decreases with $\sqrt{S}$, at low p_T $R(p_T)$ decreases with energy. In contrast, for $Q^2 = m_T^2$, $xg^{\text{EHKQS}}(x, Q^2) > xg^{\text{CTEQ61L}}(x, Q^2)$ and the enhancement decreases with energy.

Because the DGLAP gluon distributions are already well constrained by HERA data, they cannot absorb additional large effects. Therefore we conclude that, if a low-p_T enhancement in the charm cross section relative to the DGLAP-based result is observed in future experiments, it is a signal of nonlinear effects on the PDF evolution.
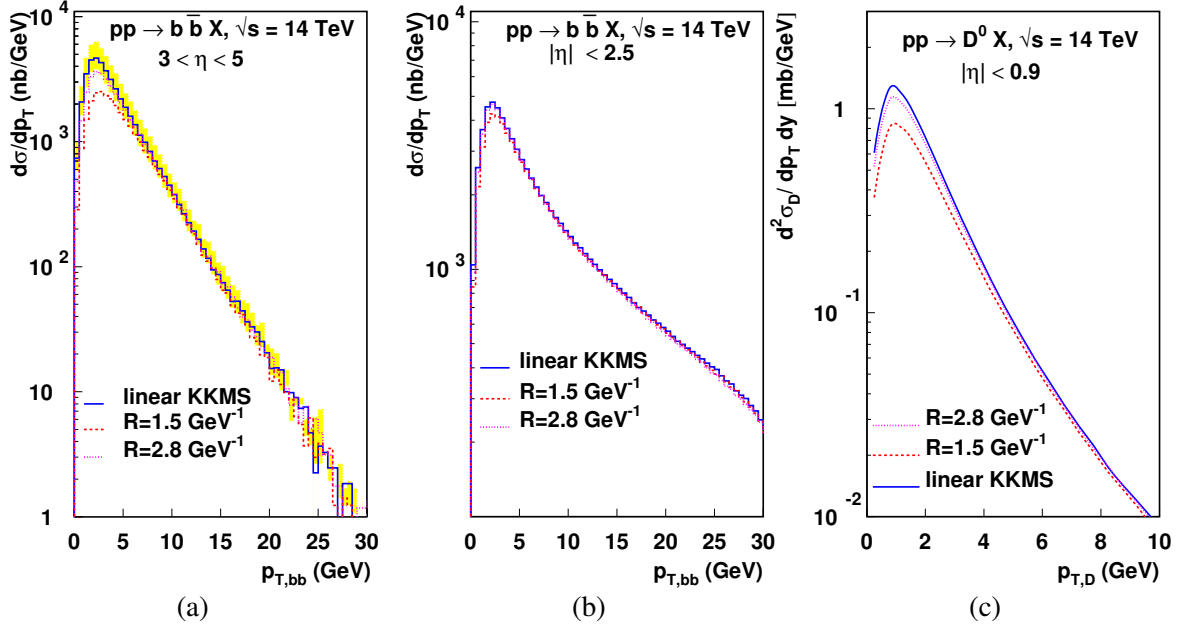
Fig. 9: (a) and (b) show $b\bar{b}$ production as a function of pair p_T without cuts in $3 < |\eta| < 5$ (a) and in the ATLAS/CMS acceptance (b). The D^0 meson p_T distribution in the ALICE acceptance is shown in (c).

4.2 BK approach[10]

Since the Tevatron measurements are well described using the unintegrated parton densities constrained by HERA and convoluted with the off-shell matrix elements, the same approach may be used for heavy quark production at the LHC at *e.g.* $\sqrt{s} = 14$ TeV. As discussed previously, see also Fig. 5, heavy quark production at this energy is already in the region where saturation effects may be relevant. In the kinematic regions, such as at the LHC, where nonlinear evolution may become important, the cross section will be suppressed due to the negative sign of the nonlinear term in Eq. (8).

First, we compute the $b\bar{b}$ production cross section at 14 TeV without any experimental cuts. In Fig. 9(a) the $b\bar{b}$ differential cross section is shown as a function of pair p_T in the forward region, $3 < |\eta| < 5$. We compare linear evolution (solid histogram), nonlinear evolution with $R = 1.5$ GeV^{-1} (dashed histogram) and $R = 2.8$ GeV^{-1} (dotted histogram). The grey band shows the uncertainty in the linear result due to the b quark mass. We take a central value of 4.75 GeV (the solid histogram) and vary m_b from 4.5 to 5 GeV. The $b\bar{b}$ pair results are shown since the pair p_T is most sensitive to the gluon k_T and thus to the saturation effects. In the hot-spot scenario, saturation effects are visible for $p_{T_{b\bar{b}}} < 5$ GeV. These saturation effects grow with rapidity, increasing the suppression to a factor of $3 - 4$ in the higher rapidity regions. For larger R, the saturation effects are not very significant.

In Fig. 9(b), the $b\bar{b}$ production cross section is computed within the ATLAS and CMS acceptance ($p_T > 10$ GeV and $|\eta| < 2.5$ for both the b and $\bar{b}$ quarks, see Ref. [74]). With these cuts, the observed suppression due to nonlinear effects nearly vanishes. This result suggests that k_T factorization can safely be applied in the central η region. Thus saturation effects due to nonlinear gluon evolution are seen only for $p_{T_{b\bar{b}}} < 10$ GeV and at high η. This regime is accessible with upgraded ATLAS/CMS detectors or in LHCb where the b quark p_T can be measured to 2 GeV for $1.9 < \eta < 4.9$. In this kinematic regime, the hot-spot scenario predicts a factor of two suppression of the $b\bar{b}$ cross section.

Similarly, we investigated $c\bar{c}$ production at ALICE. In ALICE, it will be possible to measure the D^0 down to $p_T \sim 0.5$ GeV in $|\eta| < 0.9$. The result is shown in Fig. 9(c) with $m_c = 1.5$ GeV. In the hot-spot scenario (dashed curve), a factor of two suppression occurs at $p_T \sim 1$ GeV.

---

[10]Authors: H. Jung, K. Kutak, K. Peters, L. Motyka

5 Perspectives for experimental observation at LHC[11]

5.1 Introduction

In Section 4.1, charm production in pp collisions at the LHC was suggested as a promising way to study the effects of nonlinear evolution on the parton densities. Due to gluon dominance of charm production and the small values of x and Q^2 probed, $x \approx 2 \times 10^{-4}$ and $Q^2 \approx 1.69 - 6$ GeV^2 at midrapidity and transverse momentum[12] $p_T \approx 0$, charm production at the LHC is sensitive to the gluon enhancement arising from nonlinear evolution. The resulting charm enhancement was quantified in Ref. [20, 21] by the LO ratios of the differential cross sections computed with the nonlinearly-evolved EHKQS PDFs [37], obtained from DGLAP+GLRMQ evolution, relative to the DGLAP-evolved CTEQ61L PDFs.

The enhancement of the nonlinearly-evolved gluons increases as x and Q^2 decrease. Consequently, the charm enhancement increases with center of mass energy, $\sqrt{S}$. Thus the maximum enhancement at the LHC will be at $\sqrt{S} = 14$ TeV and small charm quark transverse momentum. The sensitivity of the charm enhancement to the value of the charm quark mass, m, as well as to the choice of the factorization, Q_F^2, and renormalization, Q_R^2, scales was studied in Ref. [20, 21] assuming $Q^2 = Q_F^2 = Q_R^2 \propto m_T^2$ where $m_T^2 = p_T^2 + m^2$. The most significant charm enhancement occurs when m and Q^2/m_T^2 are both small. A comparison of the NLO total cross sections with low energy data shows that the data prefer such small m and Q^2 combinations [71, 72]. The largest enhancement is obtained with $m = 1.3$ GeV and $Q^2 = m_T^2$, see Fig. 8 in Section 4.1.

In Section 4.1, only charm enhancement was described. Neither its subsequent hadronization to D mesons nor its decay and detection were considered. In this section, we address these issues to determine whether the charm enhancement survives hadronization and decay to be measured in the ALICE detector [75]. The calculation described in that section was to leading order since the EHKQS sets are evolved according to the LO DGLAP+GLRMQ equations using a one-loop evaluation of α_s. Thus these LO distributions should generally not be mixed with NLO matrix elements and the two-loop α_s. However, the charm quark total cross section is increased and the p_T distribution is broadened at NLO relative to LO [76]. Thus, to determine whether or not the enhancement is experimentally measurable, we assume that the enhancement is the same at NLO and LO and employ a NLO cross section closest to the calculation of the enhancement in Ref. [20, 21].

As described in Ref. [76], the theoretical K factor may be defined in more than one way, depending on how the LO contribution to the cross section is calculated. In all cases, the $\mathcal{O}(\alpha_s^3)$ contribution to cross section is calculated using NLO PDFs and the two-loop evaluation of α_s. If the LO contribution is also calculated using NLO PDFs and a two-loop α_s, this is the "standard NLO" cross section. It is used in most NLO codes, both in the global analyses of the NLO PDFs and in evaluations of cross sections and rates [76]. The K factor formed when taking the ratio of the "standard NLO" cross section to the LO cross section with the NLO PDFs [76], $K_0^{(1)}$, indicates the convergence of terms in a fixed-order calculation [77]. On the other hand, if the LO contribution to the total NLO cross section employs LO PDFs and the one-loop α_s, we have a cross section which we refer to here as "alternative NLO". The K factor calculated taking the ratio of the "alternative NLO" cross section to the LO cross section with LO PDFs [76], $K_2^{(1)}$, indicates the convergence of the hadronic cross section toward a result. If $K_0^{(1)} > K_2^{(1)}$, convergence of the hadronic cross section is more likely [77]. This is indeed the case for charm production [76]. We also note that $K_2^{(1)}$ is a much weaker function of energy than $K_0^{(1)}$. Since, in the absence of nonlinear NLO PDFs, the "alternative NLO" cross section is more consistent with the calculated enhancement, we use this cross section to calculate the NLO D meson rates and p_T spectra. In both cases, the p_T distributions have the same slope even though $K_2^{(1)}$, for the alternative NLO cross section, is somewhat smaller. Thus, using a non-standard NLO calculation will not change the slope of the p_T distributions, distorting the result.

---

[11]Authors: A. Dainese and R. Vogt

[12]Here we use p_T for the transverse momentum of the charm quark and p_T^D for the transverse momentum of the D meson.

The LO and NLO calculations used to obtain the full NLO result in both cases can be defined by modification of Eq. (11) in Section 4.1. We define the full LO charm production cross section as

$$d\sigma_{\text{LO}}^{\text{1L}} = \sum_{i,j=q,\overline{q},g} f_i^{\text{LO}}(x_1, Q_F^2) \otimes f_j^{\text{LO}}(x_2, Q_F^2) \otimes d\hat{\sigma}_{ij \to c\overline{c}}^{\text{LO}}(\alpha_s^{\text{1L}}(Q_R^2), x_1, x_2) \tag{14}$$

where the superscript "LO" on $d\hat{\sigma}_{ij \to c\overline{c}}$ indicates the use of the LO matrix elements while the superscript "1L" indicates that the one-loop expression of α_s is used. The LO cross section typically used in NLO codes employs the NLO PDFs and the two-loop (2L) α_s so that

$$d\sigma_{\text{LO}}^{\text{2L}} = \sum_{i,j=q,\overline{q},g} f_i^{\text{NLO}}(x_1, Q_F^2) \otimes f_j^{\text{NLO}}(x_2, Q_F^2) \otimes d\hat{\sigma}_{ij \to c\overline{c}}^{\text{LO}}(\alpha_s^{\text{2L}}(Q_R^2), x_1, x_2) \ . \tag{15}$$

In either case, the NLO contribution, $\mathcal{O}(\alpha_s^3)$ for heavy quark production, is

$$d\sigma_{\mathcal{O}(\alpha_s^3)} = \sum_{i,j=q,\overline{q},g} f_i^{\text{NLO}}(x_1, Q_F^2) \otimes f_j^{\text{NLO}}(x_2, Q_F^2) \otimes \sum_{k=0,q,\overline{q},g} d\hat{\sigma}_{ij \to c\overline{c}k}^{\text{NLO}}(\alpha_s^{\text{2L}}(Q_R^2), Q_F^2, x_1, x_2) \tag{16}$$

where the superscript "NLO" on $d\hat{\sigma}_{ij \to c\overline{c}k}$ indicates the use of the NLO matrix elements. The additional sum over k in Eq. (16) includes the virtual ($k = 0$) and real ($k = q$, $\overline{q}$ or g depending on i and j) NLO corrections. In the calculations of $d\sigma_{\text{LO}}^{\text{2L}}$ and $d\sigma_{\mathcal{O}(\alpha_s^3)}$, we use the value of $\Lambda_{\text{QCD}}^{(4)}$ given for the NLO PDFs and work in the $\overline{\text{MS}}$ scheme. The standard NLO cross section is then

$$d\sigma_{\text{NLO}}^{\text{std}} = d\sigma_{\text{LO}}^{\text{2L}} + d\sigma_{\mathcal{O}(\alpha_s^3)} \tag{17}$$

while our "alternative NLO" cross section is defined as

$$d\sigma_{\text{NLO}}^{\text{alt}} = d\sigma_{\text{LO}}^{\text{1L}} + d\sigma_{\mathcal{O}(\alpha_s^3)} \ . \tag{18}$$

Since the enhancement in Ref. [20, 21] was defined using $d\sigma_{\text{LO}}^{\text{1L}}$ only, the best we can do is to use the alternative NLO cross section in our analysis, as described below.

We now discuss how the enhancement is taken into account in the context of the NLO computation. We calculate the LO inclusive charm p_T distribution, $d^2\sigma/dp_T dy$, with the detected charm (anticharm) quark in the rapidity interval Δy with $|y| < 1$, motivated by the pseudorapidity acceptance of the ALICE tracking barrel, $|\eta| < 0.9$. The rapidity, y_2, of the undetected anticharm (charm) quark is integrated over. The charm enhancement factor $R(p_T, \Delta y)$ is then

$$R(p_T, \Delta y) = \frac{\int_{\Delta y} dy \int dy_2 \dfrac{d^3\sigma(\text{EHKQS})}{dp_T dy dy_2}}{\int_{\Delta y} dy \int dy_2 \dfrac{d^3\sigma(\text{CTEQ61L})}{dp_T dy dy_2}} \ . \tag{19}$$

Next, we assume that the enhancement calculated at LO is the same when calculated at NLO. This is the only reasonable assumption we can make to test whether the enhancement can be detected with ALICE which will measure the physical p_T^D distribution. The alternative NLO cross section is therefore the closest in spirit to the LO computation in Ref. [20, 21]. Thus, the enhanced NLO charm p_T distribution is

$$R(p_T, \Delta y) \ d\sigma_{\text{NLO}}^{\text{alt}}(\Delta y)/dp_T \ . \tag{20}$$

Our results are obtained with the same parameters used in Section 4.1, $m = 1.2$ GeV and $Q^2 = 4m_T^2$ as well as $m = 1.3$ GeV and $Q^2 = m_T^2$. These two choices are the baseline results against which other parameter choices will be compared to see if the enhancement is detectable.

5.2   From charm to D enhancement

To make a more realistic D meson distribution, we have modified the charm p_T distribution by the heavy quark string fragmentation in PYTHIA [78]. Charm events in pp collisions at $\sqrt{S} = 14$ TeV are generated using PYTHIA (default settings) with the requirement that one of the quarks is in the interval $|y| < 1$. The charm quarks are hadronized using the default string model. Since c and $\bar{c}$ quarks fragment to D and $\overline{D}$ mesons[13], respectively, in each event related (c, D) and $(\bar{c}, \overline{D})$ pairs can easily be identified[14]. These pairs are reweighted to match an arbitrary NLO charm quark p_T distribution, dN_{NLO}^c/dp_T. If $dN_{\mathrm{PYTHIA}}^c/dp_T$ is the charm p_T distribution given by PYTHIA, each (c, D) pair is assigned the weight

$$\mathcal{W}(p_T) = \frac{dN_{\mathrm{NLO}}^c/dp_T}{dN_{\mathrm{PYTHIA}}^c/dp_T} \tag{21}$$

where p_T is the transverse momentum of the charm quark of the pair. Therefore, the reweighted final-state D distribution corresponds to the one that would be obtained by applying string fragmentation to the NLO c-quark distribution. The resulting D distribution is significantly harder than that obtained using the Peterson fragmentation function [79]. The enhancement survives after fragmentation although the D enhancement is somewhat lower than that of the charm because for a given p_T^D, the D spectrum receives contributions from charm quarks with $p_T \gtrsim p_T^D$, where the charm enhancement is smaller.

5.3   Sensitivity to the enhancement

Figure 10 shows the double-differential D^0 cross section, $d^2\sigma_D/dp_T^D dy$, in $|y| < 1$ as a function of the transverse momentum. The points represent the expected "data" measured by ALICE, obtained from the alternative NLO cross section scaled by the enhancement factor $R(p_T, \Delta y)$ defined in Eq. (19), and modified by string fragmentation. The solid and dashed curves are obtained by applying string fragmentation to the alternative NLO and standard NLO $c\bar{c}$ cross sections, respectively. Thus, the "data" points include the enhancement while the curves do not. The horizontal error bars indicate the bin width, the vertical error bars represent the statistical error and the shaded band gives the p_T-dependent systematic error. The 5% p_T-independent systematic error on the normalization is not shown. (See Ref. [80] for a discussion of the error analysis. The standard NLO cross section, Eq. (17), and the $\mathcal{O}(\alpha_s^3)$ contribution to the alternative NLO cross section, Eq. (16), were calculated using the HVQMNR code [81] with CTEQ6M and $\Lambda_{\mathrm{QCD}}^{(4)} = 0.326$ GeV. The LO contribution to the alternative NLO cross section, Eq. (14), was calculated using the CTEQ61L PDFs. Fragmentation was included as described in Section 5.2. The enhancement, the difference between the data and the solid curves for $p_T^D \lesssim 3$ GeV, is more pronounced for the larger mass and lower scale, on the right-hand side of Fig. 10.

There is a significant difference between the alternative and standard NLO distributions. Part of the difference is due to the one- and two-loop evaluations of α_s since $\alpha_s^{2L} < \alpha_s^{1L}$. However, the most important contribution is the large differences between the LO and NLO gluon distributions, especially at low scales [80].

In order to address the question of the experimental sensitivity to the effect of nonlinear gluon evolution on low-p_T charm production, we consider, as a function of p_T^D, the ratio of the simulated data, including the enhancement, to alternative NLO calculations using a range of m and Q^2 with PYTHIA string fragmentation. We denote this ratio as "Data/Theory" and try to reproduce this ratio with NLO calculations employing recent linearly-evolved PDFs and tuning m and Q^2.

Since the enhancement has disappeared for $p_T^D \gtrsim 5$ GeV, we refer to this unenhanced region as high p_T^D. The p_T^D region below 5 GeV, where the enhancement is important, is referred to as low p_T^D. If no set of parameters can describe both the high- and low-p_T^D components of the distribution equally

---

[13]Here $D \equiv D^+, D^0$.

[14]Events containing charm baryons were rejected.
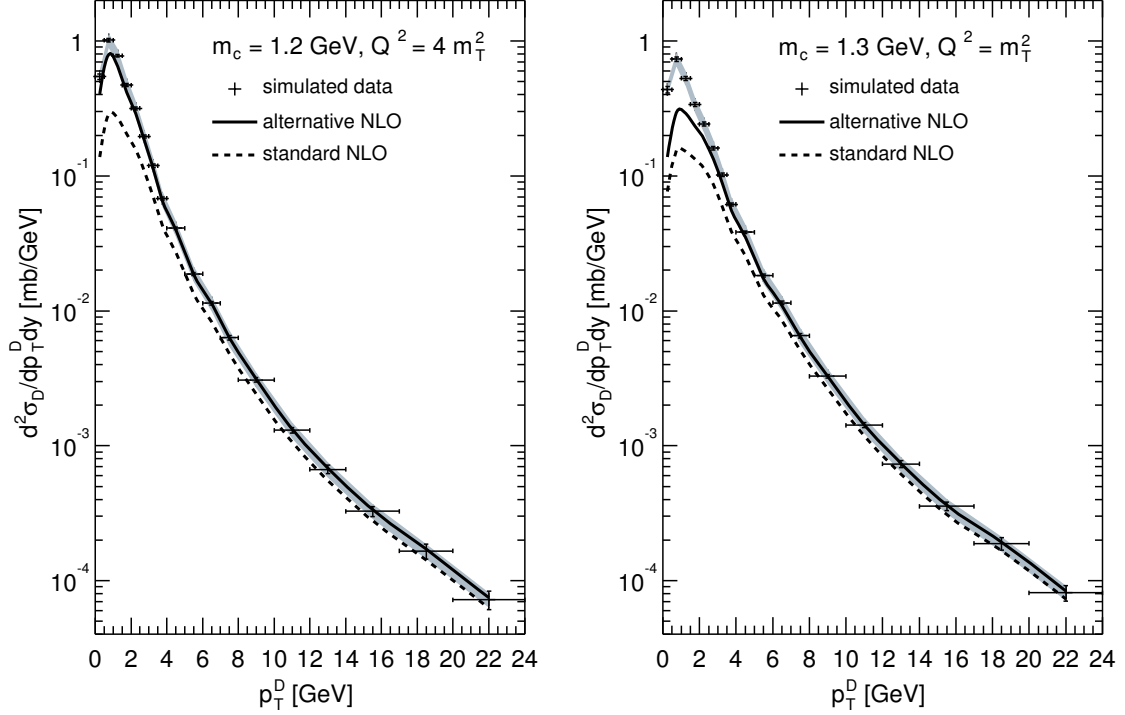
Fig. 10: Comparison of the simulated ALICE data generated from $R(p_T, \Delta y)d\sigma_{\mathrm{NLO}}^{\mathrm{alt}}$ with the alternative (solid) and standard (dashed) NLO calculations. The effect of string fragmentation is included in the "data" points as well as in the curves. The left-hand side shows the result for $m = 1.2$ GeV and $Q^2 = 4m_T^2$ while the right-hand side is the result for $m = 1.3$ GeV and $Q^2 = m_T^2$. The error bars on the data represent the statistical error and the shaded band represents the p_T-dependent systematic error. The 5% normalization error is not shown.

well, and, if the set that best reproduces the high-p_T^D part underestimates the low-p_T^D part, this would be a strong indication of the presence of nonlinear effects.

The Data/Theory plots are shown in Fig. 11. The points with the statistical (vertical bars) and p_T-dependent systematic (shaded region) error correspond to the data of Fig. 10, including the enhancement, divided by themselves, depicting the sensitivity to the theory calculations. The black squares on the right-hand sides of the lines Data/Theory $= 1$ represent the 5% p_T-independent error on the ratio coming from the cross section normalization. This error is negligible relative to present estimates of other systematic uncertainties ($\simeq 13\%$).

On the left-hand side, the thick solid curve with $m = 1.2$ GeV and $Q^2 = 4m_T^2$ best agrees with the high-p_T^D ratio by construction since $R \approx 1$ at large p_T^D. It also shows the effect of the enhancement well beyond the error band for $p_T^D \lesssim 2$ GeV. Better agreement with the data over the entire p_T^D range can be achieved only by choosing a charm quark mass lower than 1.2 GeV, below the nominal range of charm masses, as illustrated by the dashed curve for $m = 1.1$ GeV. Higher masses with $Q^2 = 4m_T^2$ produce much larger Data/Theory ratios than the input distribution. The ratio with $m = 1.3$ GeV and $Q^2 = m_T^2$ (dot-dot-dashed curve) gives a much larger ratio at low p_T^D and drops below ≈ 1 for $p_T^D > 8$ GeV.

We also present the ratio using the MRST parton densities (MRST2001 LO [36] in Eq. (14) and MRST2002 NLO [82] in Eq. (16)) with $m = 1.2$ GeV and $Q^2 = 4m_T^2$. We find that this result also agrees reasonably well with the CTEQ6 results for the same m and Q^2. Thus, the enhancement seems to be rather independent of the PDF. The CTEQ61L and the MRST2001 LO distributions are similar at low x, suggesting that non-linearly evolved PDFs based on MRST2001 LO would produce an enhancement like that of Ref. [20, 21].
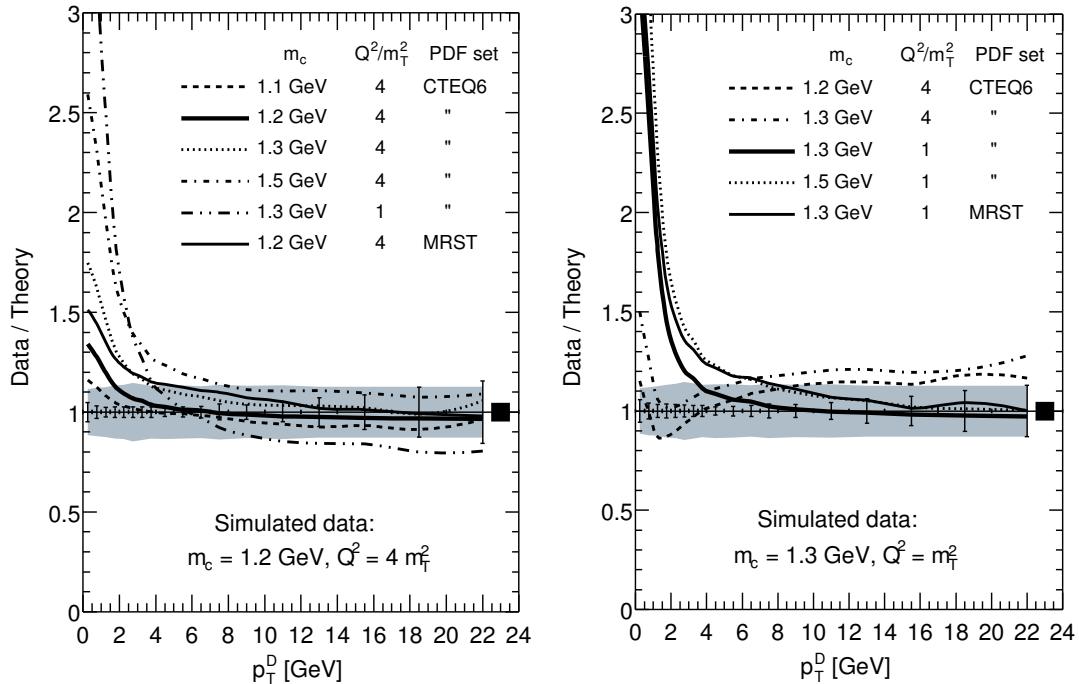
Fig. 11: Ratio of the generated ALICE data relative to calculations of the alternative NLO cross sections with several sets of parameters and PYTHIA string fragmentation. The left-hand side shows the result for $m = 1.2$ GeV and $Q^2 = 4m_T^2$ while the right-hand side is the result for $m = 1.3$ GeV and $Q^2 = m_T^2$.

On the right-hand side of Fig. 11 the thick solid curve, employing the same parameters as the data, gives the best agreement at high p_T^D. We note that even though the results with $Q^2 = 4m_T^2$ and $m \leq 1.3$ GeV lie closer to the data at low p_T^D and within the combined statistical and systematic error at higher p_T^D, the curves with these parameters have the wrong slopes for $p_T^D \lesssim 8$ GeV. The statistical sensitivity is expected to be good enough to distinguish the difference in curvature. The results with the MRST PDFs do not alter the conclusions.

5.4 Conclusions

We have studied whether the EHKQS gluon distributions [37] could generate an observable D meson enhancement in pp collisions at the LHC. Using the EHKQS LO PDFs and LO matrix elements for charm quark production and PYTHIA string fragmentation for D meson hadronization, the enhancement indeed survives to the D mesons.

The D meson enhancement, however, drops rapidly with transverse momentum. Therefore, D measurement capability at small p_T^D is necessary to verify the effect experimentally. The ALICE detector can directly reconstruct $D^0 \rightarrow K^-\pi^+$. We have demonstrated that, in the most optimistic case, the enhancement can be detected above the experimental statistical and systematic errors. When the charm mass is somewhat smaller, $m = 1.2$ GeV, but the scale is larger, $Q^2 = 4m_T^2$, it is more difficult to detect the enhancement over the experimental uncertainties.

Acknowledgements

References

[1] Yu. L. Dokshitzer, Sov. Phys. JETP **46**, 641 (1977).

[2] V. N. Gribov, and L. N. Lipatov, Sov. J. Nucl. Phys. **15**, 438 (1972).

[3] V. N. Gribov and L. N. Lipatov, Sov. J. Nucl. Phys. **15**, 675 (1972).

[4] G. Altarelli and G. Parisi, Nucl. Phys. **B 126**, 298 (1977).

[5] L. N. Lipatov, Sov. J. Nucl. Phys. **23**, 338 (1976).

[6] E. A. Kuraev, L. N. Lipatov and V. S. Fadin, Sov. Phys. JETP **44**, 443 (1976).

[7] I. I. Balitsky and L. N. Lipatov, Sov. J. Nucl. Phys. **28**, 822 (1978).

[8] L. N. Lipatov, Sov. Phys. JETP **63**, 904 (1986).

[9] M. Ciafaloni, D. Colferai, G. P. Salam and A. M. Stasto, Phys. Lett. **B 576**, 143 (2003).

[10] M. Ciafaloni, D. Colferai, G. P. Salam and A. M. Stasto, Phys. Rev. **D 68**, 114003 (2003).

[11] R. S. Thorne, Phys. Lett. **B 474**, 372 (2000).

[12] R. S. Thorne, Phys. Rev. **D 64**, 074005 (2001).

[13] G. Altarelli, R. D. Ball and S. Forte, Nucl. Phys. **B 674**, 459 (2003).

[14] V. A. Khoze, A. D. Martin, M. G. Ryskin and W. J. Stirling, Phys. Rev. **D 70**, 074013 (2004).

[15] G. P. Salam, arXiv:hep-ph/0501097 (2005).

[16] A. Donnachie and P. V. Landshoff, Phys. Lett. **B 296**, 227 (1992).

[17] J. Pumplin et al., JHEP **07**, 012 (2002).

[18] A. D. Martin, R. G. Roberts, W. J. Stirling and R. S. Thorne, Phys. Lett. **B 604**, 61 (2004).

[19] A. D. Martin, M. G. Ryskin and G. Watt, Phys. Rev. **D 70**, 091502 (2004).

[20] K. J. Eskola, V. J. Kolhinen and R. Vogt, Phys. Lett. **B 582**, 157 (2004).

[21] K. J. Eskola, V. J. Kolhinen and R. Vogt, J. Phys. **G 30**, S1171 (2004).

[22] L. V. Gribov, E. M. Levin and M. G. Ryskin, Phys. Rept. **100**, 1 (1983).

[23] A. H. Mueller and J.-W. Qiu, Nucl. Phys. **B 268**, 427 (1986).

[24] I. Balitsky, Nucl. Phys. **B 463**, 99 (1996).

[25] Yu. V. Kovchegov, Phys. Rev. **D 60**, 034008 (1999).

[26] J. Bartels, Phys. Lett. **B 298**, 204 (1993).

[27] J. Bartels, Z. Phys. **C 60**, 471 (1993).

[28] J. Bartels and M. Wusthoff, Z. Phys. **C 66**, 157 (1995).

[29] A. D. Martin, R. G. Roberts, W. J. Stirling and R. S. Thorne, Eur. Phys. J. **C 35**, 325 (2004).

[30] J. Huston, J. Pumplin, D. Stump and W. K. Tung, arXiv:hep-ph/0502080 (2005).

[31] R. S. Thorne, A. D. Martin, R. G. Roberts and W. J. Stirling, arXiv:hep-ph/0507015 (2005).

[32] CDF Coll., D. Acosta et al., Phys. Rev. **D 71**, 032001 (2005).

[33] A. D. Martin, R. G. Roberts and W. J. Stirling, Phys. Rev. **D 37**, 1161 (1988).

[34] LHCb Coll., Z. J. Ajaltouni et al., Nucl. Phys. Proc. Suppl. **115**, 297 (2003).

[35] H. L. Lai et al., Eur. Phys. J. **C 12**, 375 (2000).

[36] A. D. Martin, R. G. Roberts, W. J. Stirling and R. S. Thorne, Eur. Phys. J. **C 23**, 73 (2002).

[37] K. J. Eskola, H. Honkanen, V. J. Kolhinen, J.-W. Qiu and C. A. Salgado, Nucl. Phys. **B 660**, 211 (2003).

[38] H1 Coll., C. Adloff et al., Eur. Phys. J. **C 21**, 33 (2001).

[39] K. Prytz, Phys. Lett. **B 311**, 286 (1993).

[40] I. Balitsky, Phys. Rev. Lett. **81**, 2024 (1998).

[41] I. Balitsky, Phys. Rev. **D 60**, 014020 (1999).

[42] I. Balitsky, Phys. Lett. **B 518**, 235 (2001).

[43] E. A. Kuraev, L. N. Lipatov and V. S. Fadin, Sov. Phys. JETP **45**, 199 (1977).

[44] A. Kovner, J. G. Milhano and H. Weigert, Phys. Rev. **D 62**, 114005 (2000).

[45] J. Bartels and K. Kutak, *Momentum space analysis of the triple pomeron vertex*, 2005. In preparation.

[46] M. Ciafaloni, Nucl. Phys. **B 296**, 49 (1988).

[47] S. Catani, F. Fiorani and G. Marchesini, Phys. Lett. **B 234**, 339 (1990).

[48] S. Catani, F. Fiorani and G. Marchesini, Nucl. Phys. **B 336**, 18 (1990).

[49] G. Marchesini, Nucl. Phys. **B 445**, 49 (1995).

[50] J. Kwiecinski, A. D. Martin and A. M. Stasto, Phys. Rev. **D 56**, 3991 (1997).

[51] M. A. Kimber, J. Kwiecinski and A. D. Martin, Phys. Lett. **B 508**, 58 (2001).

[52] K. Kutak and J. Kwiecinski, Eur. Phys. J. **C 29**, 521 (2003).

[53] K. Kutak and A. M. Stasto, Eur. Phys. J. **C 41**, 343 (2005).

[54] B. Andersson, G. Gustafson, H. Kharraziha and J. Samuelsson, Z. Phys. **C 71**, 613 (1996).

[55] J. Kwiecinski, A. D. Martin and P. J. Sutton, Z. Phys. **C 71**, 585 (1996).

[56] G. P. Salam, JHEP **07**, 019 (1998).

[57] G. P. Salam, Acta Phys. Polon. **B 30**, 3679 (1999).

[58] M. Ciafaloni, D. Colferai and G. P. Salam, Phys. Rev. **D 60**, 114036 (1999).

[59] M. Ciafaloni and D. Colferai, Phys. Lett. **B 452**, 372 (1999).

[60] H1 Coll., C. Adloff et al., Phys. Lett. **B 528**, 199 (2002).

[61] ZEUS Coll., J. Breitweg et al., Eur. Phys. J. **C 12**, 35 (2000).

[62] H. Jung, Comput. Phys. Commun. **143**, 100 (2002).

[63] H. Jung and G. P. Salam, Eur. Phys. J. **C 19**, 351 (2001).

[64] ZEUS Coll., S. Chekanov et al., Eur. Phys. J. **C 21**, 443 (2001).

[65] CDF Coll., D. Acosta et al., Phys. Rev. **D 71**, 032001 (2005).

[66] CDF Coll., D. Acosta et al., Phys. Rev. **D 71**, 092001 (2005).

[67] D0 Coll., B. Abbott et al., Phys. Lett. **B 487**, 264 (2000).

[68] M. Cacciari, S. Frixione, M. L. Mangano, P. Nason and G. Ridolfi, JHEP **07**, 033 (2004).

[69] D. Stump et al., JHEP **10**, 046 (2003).

[70] A. D. Martin, R. G. Roberts, W. J. Stirling and R. S. Thorne, Eur. Phys. J. **C 4**, 463 (1998); A. D. Martin, R. G. Roberts, W. J. Stirling and R. S. Thorne, Phys. Lett. **B 443**, 301 (1998).

[71] R. Vogt, Int. J. Mod. Phys. **E 12**, 211 (2003).

[72] R. Vogt, *In proceedings of the 18$^{\text{th}}$ Winter Workshop on Nuclear Dynamics, edited by R. Bellwied et al., Nassau, The Bahamas, p. 253*. EP Systema, Debrecen, Hungary, 2002. [arXiv:hep-ph/0203151].

[73] Vogt, R., Z. Phys. **C 71**, 475 (1996).

[74] O. Behnke et al., *Experimental overview*. These proceedings.

[75] ALICE Coll., *Technical proposal*, 1995. CERN/LHCC 95-71.

[76] R. Vogt, Heavy Ion Phys. **17**, 75 (2003).

[77] N. Kidonakis, E. Laenen, S. Moch and R. Vogt, Phys. Rev. **D 67**, 074037 (2003).

[78] T. Sjostrand et al., Comput. Phys. Commun. **135**, 238 (2001).

[79] C. Peterson, D. Schlatter, I. Schmitt and P. M. Zerwas, Phys. Rev. **D 27**, 105 (1983).

[80] A. Dainese, R. Vogt, M. Bondila, K. J. Eskola and V. J. Kolhinen, J. Phys. **G 30**, 1787 (2004).

[81] M. L. Mangano, P. Nason and G. Ridolfi, Nucl. Phys. **B 373**, 295 (1992).

[82] A. D. Martin, R. G. Roberts, W. J. Stirling and R. S. Thorne, Phys. Lett. **B 531**, 216 (2002).